

Swift-BAT Survey of Galactic Sources: Catalog and Properties of the populations

R. Voss¹

Max Planck Institut für Extraterrestrische Physik, P.O. Box 1603, 85740, Garching, Germany

`rvoss@mpe.mpg.de`

and

M. Ajello

SLAC National Accelerator Laboratory and Kavli Institute for Particle Astrophysics and Cosmology, 2575 Sand Hill Rd, Menlo Park, CA 94304, USA

ABSTRACT

We study the populations of X-ray sources in the Milky Way in the 15-55 keV band using a deep survey with the *BAT* instrument aboard the *Swift* observatory. We present the logN-logS distributions of the various source types and we analyze their variability and spectra. For the low-mass X-ray binaries (LMXBs) and the high-mass X-ray binaries (HMXBs) we derive the luminosity functions to a limiting luminosity of $L_X \sim 7 \times 10^{34}$ erg s⁻¹. Our results confirm the previously found flattening of the LMXB luminosity function below a luminosity of $L_X \sim 10^{37}$ erg s⁻¹. The luminosity function of the HMXBs is found to be significantly flatter in the 15-55 keV band than in the 2-10 keV band. From the luminosity functions we estimate the ratios of the hard X-ray luminosity from HMXBs to the star-formation rate, and the LMXB luminosity to the stellar mass. We use these to estimate the X-ray emissivity in the local universe from X-ray binaries and show that it constitutes only a small fraction of the hard X-ray background.

Subject headings: Galaxy: stellar content – X-rays: binaries – X-rays: stars

1. Introduction

Large galaxies typically contains hundreds of bright ($> 10^{36}$ erg s⁻¹) X-ray sources, of which the majority are high-mass X-ray binaries (HMXBs) or low-mass X-ray binaries (LMXBs). The possibilities of studying them in external galaxies with *XMM-Newton* and *Chandra* have sparked interest in studying the populations of these sources in galaxies. The Milky Way provides a useful reference for such studies. Besides a considerable population of HMXBs in the Magellanic clouds (e.g. Liu et al. 2005), and the detection of a few individual sources in other nearby galaxies (e.g. Pietsch et al. 2006), the Milky Way is the only

galaxy in which it is currently, or in the near future, possible to obtain information on a high fraction of the X-ray binaries from measurements in other wavebands than the X-rays. It is also possible to measure X-ray sources in the Milky Way at much lower luminosities than in external galaxies. The X-ray source populations in the Milky Way can therefore provide us with unique observational constraints.

However, the analysis of the population of X-ray sources in the Galaxy suffer from several problems. The Galaxy has a large angular size and the distances to many of the sources are not known. The population of sources is mixed and from X-rays alone it is not always possible to distinguish a weak nearby source from a more distant bright source. Focusing telescopes have small fields of

¹Excellence Cluster Universe, Technische Universität München, Boltzmannstr. 2, D-85748, Garching, Germany

view and are therefore not suited for such studies. Grimm et al. (2002) used the All-Sky Monitor (ASM) of the RXTE observatory to study the populations of X-ray sources in the 2-10 keV band, and constrained the luminosity functions of X-ray binaries with luminosities $\gtrsim 10^{36}$ erg s $^{-1}$. They found that the differential luminosity function of the HMXBs could be approximated by a single power-law with a slope of $\Gamma \simeq -1.6$, whereas the luminosity function of LMXBs was more complicated with a steep slope at high luminosities and a shallow slope at luminosities below 10^{37} erg s $^{-1}$. With *XMM-Newton* and *Chandra* the investigations were extended to also cover nearby galaxies. Grimm et al. (2003) found that the luminosity function of HMXBs in a sample of star-forming galaxies showed no evidence of variation, and was consistent with the results from the Milky Way slope of $\Gamma \simeq -1.6$, with a possible cut-off at very high luminosities, a few $\times 10^{40}$ erg s $^{-1}$. Investigations of the LMXB populations in old stellar environments also found results consistent with the Milky Way results, with a steep slope at high luminosities and a shallower slope at lower luminosities (e.g. Kim & Fabbiano 2004; Voss & Gilfanov 2006, 2007; Kim et al. 2009). However, the exact shape remains controversial. Gilfanov (2004) combined results from nearby galaxies with those of the Milky Way and found a power-law slope of $\Gamma \simeq -1.0$ at luminosities below 10^{37} erg s $^{-1}$, and a slope of $\Gamma \simeq -1.8$ above this limit, breaking to an even steeper slope at luminosities above 5×10^{38} erg s $^{-1}$. Kim & Fabbiano (2004) studied a larger sample of galaxies, and confirmed the slope of $\Gamma \simeq -1.8$ at luminosities above a few times 10^{37} erg s $^{-1}$, and while a single power-law fit was acceptable, the fit did improve when a break to a steeper slope at high luminosities was included. Studies of the bulge of M31 and the early type galaxy Centaurus A (Cen A, NGC 5128) showed a clear break at low luminosities $\sim 10^{37}$ erg s $^{-1}$ confirming the low-luminosity slope of $\Gamma \simeq -1.0$ (Voss & Gilfanov 2006, 2007; Voss et al. 2009). While initial studies of the elliptical galaxies NGC 3379 and NGC 4278 (Kim et al. 2006) did not show any evidence of this break, deeper observations indicate some flattening towards low luminosities (Kim et al. 2009). Finally, recent results (Voss & Gilfanov 2007; Woodley et al. 2008; Voss et al. 2009; Kim et al.

2009) show that there is a difference between the luminosity functions of LMXBs in globular clusters and those outside, with a dearth of low-luminosity sources in globular clusters.

The *RXTE ASM*, *Chandra* and *XMM-Newton* observatories are only detecting photons below ~ 10 keV. However, many X-ray binaries emit a significant fraction of their energy in harder X-rays. Incomplete knowledge of the different X-ray states, and the time individual sources stay in these states, makes it difficult to extrapolate the observations below 10 keV to wider bands. Furthermore these telescopes are biased against objects with high absorbing column densities $> 10^{22}$ cm $^{-2}$ (see e.g. Figure 3 in Ajello et al. 2009), such as the very absorbed HMXBs recently discovered with *INTEGRAL* (e.g. Walter et al. 2006). The first observatory useful for population studies of the Milky Way in hard X-rays (> 10 keV) was *INTEGRAL* with its coded-mask telescopes. This capability was used by Lutovinov et al. (2005) to study the spectra and spatial distribution of the Galactic population of HMXBs. A similar study of the LMXBs, including the luminosity function, was carried out by Revnivtsev et al. (2008), but this study was limited to the bulge LMXBs.

In this paper we extend the study of the populations of Galactic X-ray sources in the hard X-rays, utilizing data obtained by the *Burst Alert Telescope* (BAT; Barthelmy et al. 2005), on board the *Swift* satellite (Gehrels et al. 2004). We follow the approach of Grimm et al. (2003), compiling a catalogue of sources based on previously published identifications. These are then analyzed taking into account the limits of the identification procedures.

2. The BAT X-ray Survey

The *BAT* represents a major improvement in sensitivity for imaging of the hard X-ray sky. BAT is a coded mask, wide field of view, telescope sensitive in the 15–200 keV energy range. BAT's main purpose is to locate Gamma-Ray Bursts (GRBs). While chasing new GRBs, BAT surveys the hard X-ray sky with an unprecedented sensitivity. Thanks to its wide FOV and its pointing

strategy, *BAT* monitors continuously up to 80% of the sky every day. Therefore the light-curves of all sources are sampled regularly in a manner similar to the *RXTE ASM*. Many X-ray sources are highly variable on a variety of timescales, and therefore regular sampling is important for deriving the average properties of objects, as opposed to pointed observations that are useful for deriving the physical properties of objects at specific times. Results of the *BAT* survey (Markwardt et al. 2005; Ajello et al. 2008a) show that *BAT* reaches a sensitivity of ~ 1 mCrab in 1 Ms of exposure except near bright sources or very crowded fields, where the high backgrounds can worsen the sensitivity by a factor of ~ 2 . Given its sensitivity and the large exposure already accumulated in the whole sky, *BAT* poses itself as an excellent instrument for studying the Galactic source populations.

2.1. Data Processing

For the analysis presented here, we used all the available *BAT* data taken from January 2005 to March 2007. The chosen energy range for the all-sky analysis is 15–55 keV. The lower limit is dictated by the energy threshold of the detectors. The upper limit was chosen as to avoid the presence of strong background lines which could worsen the overall sensitivity. Data were processed using standard Swift software contained in the HEASOFT 6.3.2 distribution. Data screening was performed according to Ajello et al. (2008a). We recall here the main steps. Data are filtered according to the stability of the pointing, the *BAT* array rate (≤ 18000 Hz), the distance to the South Atlantic Anomaly, the goodness of the fit to the *BAT* array background ($\chi_{red} < 1.5$) and the presence of known sources at the correct position in the FOV. Only those data which fulfill these criteria are used for the analysis. The main difference from Ajello et al. (2008a) is that we integrate over energy in the 15–55 keV band instead that in the 14–170 keV band. The all-sky image is obtained as the weighted average of all the shorter (per-pointing) observations. For this analysis, we consider only the sky region along the Galactic Plane whose absolute Galactic latitude is less than 20° . The average exposure in the Galactic region is 2.6 Ms, being 1.3 Ms and 4.1 Ms the minimum and maximum exposure times respectively. The final image shows a Gaussian normal noise and we

identified source candidates as excesses above the 4.8σ level. Above this threshold, we detected 228 objects. Considering that the all-sky image has a pixel size of 8×8 arcmin for a total of 2.25 million pixels, we expect ~ 1.8 spurious detection above the 4.8σ threshold ($\leq 1\%$ of the total number of excesses).

All the candidates are fit with the *BAT* point spread function (using the standard *BAT* tool *batcelldetect*) to derive the best source position. The sources found in this way are all those whose averaged emission is above the sensitivity limit of our survey ($\sim 1 - 2 \times 10^{-11}$ erg cm $^{-2}$ s $^{-1}$ in the 15–55 keV band, depending on the local exposure and background) at the position of the source. Fast transients, which are detected in the per-pointing analysis only, are not discussed here and their study will be left to a future publication.

2.2. Source Identification

We used high-energy catalogs in order to identify *BAT* sources. Identification was in most cases a straightforward process, since the cross-correlation of *BAT* objects with the ROSAT All-Sky Survey Bright Source Catalogue (Voges et al. 1999) provides an easy and solid way to identify a large fraction ($\sim 70\%$) of them (Ajello et al. 2008a). Most of the uncorrelated sources are not present in the ROSAT survey because of absorption (either along the line of sight or intrinsic to the source). However, given the very large exposure INTEGRAL accumulated along the Galactic plane, most of the remaining sources were identified using the Third IBIS Catalog (Bird et al. 2007) and the INTEGRAL all-sky catalog (Krivonos et al. 2007).

We report in Fig. 1, the offset of the *BAT* sources from the catalogued counterpart as a function of S/N. We determine that the mean offset varies with significance according to

$$\text{OFFSET} = (6.1 \pm 1.5) \times (S/N)^{-0.56(\pm 0.20)} + 0.13 \quad (\text{arcmin}), \quad (1)$$

where the constant of 0.13' is due to a systematic misalignment of the boresight which causes the systematic offset of the brightest sources (see also Tueller et al. 2010). At the detection threshold of 4.8σ the average offset is $\sim 2.6'$. Moreover, Fig. 1 shows the standard deviation of the data for different logarithmic bins of source signif-

icance. This is found to be always less than $2.5'$. Moreover, Figure 2 shows the difference in the celestial coordinates between the position of the BAT sources and the position of the optical counterpart. In both directions (e.g. right ascension and declination) the distributions are centered in zero and exhibit a similar standard deviation of $1.5'$. All these results confirm the good position accuracy of BAT even in crowded regions as the Galactic plane.

3. Catalog

In Table 1 we report the coordinates, fluxes and other details of the 228 detected sources. Most of the objects have both an identification in other X-ray band and in the optical. In a few cases, the optical classification is still uncertain or unknown. Only in 5 cases we do not have a secure identification for the BAT object, and 12 further sources do have counterparts, but have unidentified object types. For 4 of the 5 sources without identification we have listed tentative IDs in Table 2. The fluxes quoted in Table 1 are time-averaged fluxes over the whole data set in the 15–55 keV energy band. Conversion from count rate to flux was performed adopting a Crab Nebula spectrum of the form $dN/dE = 10.17 E^{-2.15}$. Position uncertainty for the BAT objects can be derived, as a function of significance, using Equation 1. We derive that the average location accuracy for a 5, 10 and 20σ source is $2.6'$, $1.8'$ and $1.2'$. For comparison, the location accuracies reported for INTEGRAL-IBIS for the same significances are $2.1'$, $1.5'$ and $0.8'$ respectively (Krivonos et al. 2007). The better location accuracy of INTEGRAL-IBIS is not surprising in view of the fact that the IBIS point spread function is sharper than the BAT one ($12'$ versus $22'$ full width at half maximum, see Bird et al. 2006; Barthelmy et al. 2005).

Many of the X-ray binaries have known distances, albeit with large uncertainties, and the catalogue includes the approximate distances to HMXBs taken from Liu et al. (2006) and to LMXBs from Liu et al. (2007). In Table 3 we give the numbers of different identified source types, and in Figure 3 the distribution of the source types on the sky is shown.

Figure 4 shows the inner $20^\circ \times 10^\circ$ region around the Galactic center where BAT detects more than

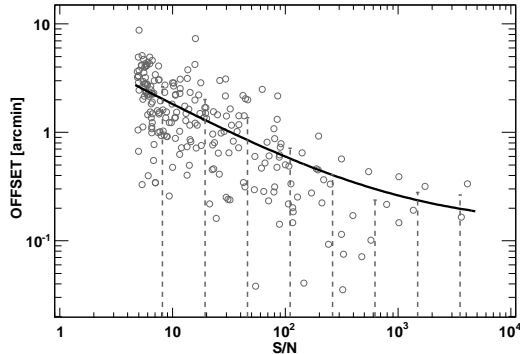


Fig. 1.— Offset from catalog position for the sources reported in Table 1 as a function of S/N (open circles). The solid line represents the best fit to the data (see Eq. 1) and gives the mean offset vs. S/N. The dashed lines show the standard deviation of the offset distribution in several bins of S/N.

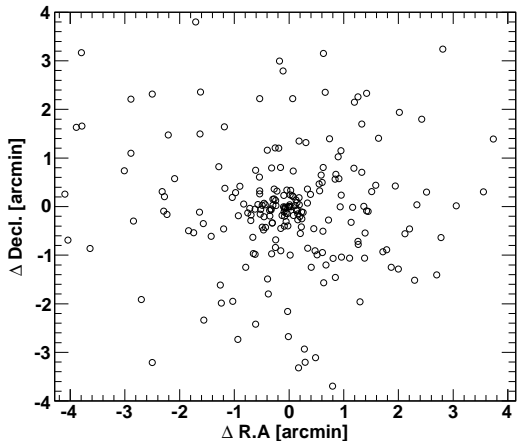


Fig. 2.— Difference in right ascension and declination between the positions of the BAT sources and the position of their optical counterparts.

30 sources. Particularly, when looking at the Galactic center, the similarity of the BAT and the INTEGRAL images is apparent (Revnivtsev et al. 2004; Bird et al. 2006) although BAT is unable to resolve all the sources in this complex region. Two of the sources reported in the map are not part of this work because their significance, when integrated over the 2 years of the survey, is lower than 4.8σ . Indeed, they are transient sources which are detected by BAT only during their outburst episodes. One source is XTE J1747-274 which is a neutron star LMXB which was very active particularly in March-April 2005 (see e.g. Zhang et al. 2009, and references therein). The other source, IGR J17391-3021, is a supergiant fast X-ray transient characterized by very short intense bursts lasting on the order of hours (e.g. Smith et al. 2006). This source was particularly active in BAT during 2006.

4. Spectral Properties

For each object in our survey we extracted a 15–195 keV spectrum with the method described in Ajello et al. (2008c). Here we recall the main steps: for a given source, we extract a spectrum from each observation where the source is in the field of view. These spectra are corrected for residual background contamination and for vignetting; the per-pointing spectra are then (weighted) averaged to produce the final source spectrum. Thus, the final spectrum represents the average source emission over the time-span considered here. The accuracy of these spectra is discussed in details in Ajello et al. (2009).

The average spectral properties of the sample can be studied by means of hardness ratios (HR) which are defined as normalized differences between the background-subtracted count-rates in the soft band (S, 14–22 keV), in the medium band (M, 22–50 keV) and in the hard band (H, 50–195 keV).

These HRs are defined respectively as:

$$HR_1 = \frac{M - H}{M + H}, \quad HR_2 = \frac{S - H}{S + H}, \quad (2)$$

The hardness ratios, shown in Fig. 5, are normalized to the range -1 and +1 setting negative count-rates to zero.¹ In this plot, hard power-law sources

(e.g. AGNs) occupy the central part of the diagram while soft sources tend to move to positive values of HR_1 . All the detected sources reported in Tab. 1 are also shown in Fig. 5 (i.e. no sources have been excluded from the graph) and this is due to the fact that BAT is able to constrain efficiently the source spectrum even in the hard band (50–195 keV). While it is noticeable that all Galactic sources are generally softer than AGNs, a striking feature is the clustering of 20 LMXBs at large values of both HR_1 and HR_2 . The combination of the two points to the fact that these sources exhibit an extremely soft spectrum below 50 keV and an hard spectrum above this energy. To investigate this more in details we created a stacked spectrum of LMXBs with $HR_2 > 0.6$ and < 0.6 . These are shown in Fig. 6 along with the best-fit models. Indeed LMXBs clustering in the upper-right corner of the HR plot exhibit a spectrum which is dominated by a bright black body component ($kT=2.70\pm 0.70$ keV) at low energy and by a flat power law (index of 1.6 ± 0.4) at high energy. This corresponds to the high/soft state typical of bright LMXBs. On the other hand, all the other LMXBs are characterized by a power-law type spectrum with a photon index of 2.74 ± 0.06 , corresponding to the low/hard state. The analysis of the stacked spectra of all Galactic source classes (with more than 5 objects) is reported in Table 4. From this analysis it is evident that most Galactic sources have a non-negligible hard X-ray emission which extends all the way up to 200 keV and that can be modeled as a power law. The only exception is represented by the CV class whose average spectrum is softer than a power law and consistent with a bremsstrahlung model with a temperature of ~ 22 keV (see e.g. Brunschweiler et al. 2009). The stacked spectrum of all the CVs (19) detected by BAT is reported in Fig. 7.

positions showed that, in each energy channel, the count-rates are found consistent with zero within errors. Thus, a few negative count-rates consistent with zero (particularly at high energy) can be interpreted as a non-detection of the source in that band. However, as a test we allowed negative count-rates to exist and we found that only 3 objects have an hardness ratio value which falls outside the above range. All these objects are LMXBs with basically no detection in the hard-band. Thus, the results reported below do not change whether negative count-rates are set to zero or not.

¹As shown in Ajello et al. (2009), the analysis of off-source

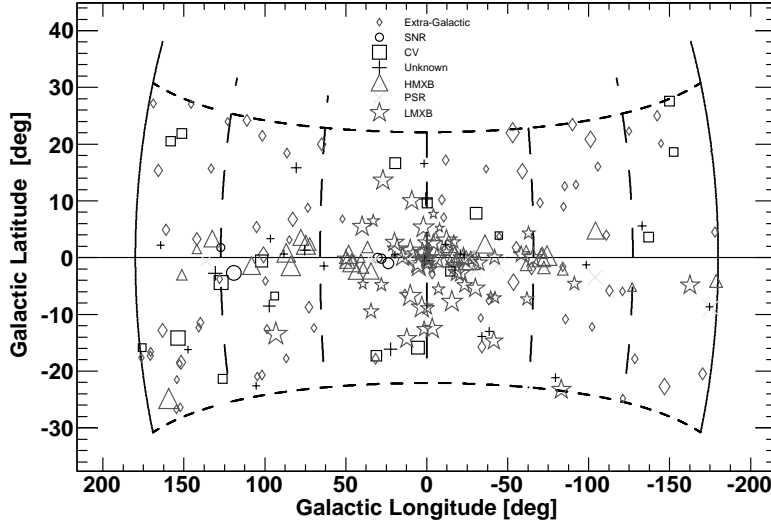


Fig. 3.— AITOFF projection of the distribution of sources on the sky, divided by source type. The size of the symbols is proportional to the source flux.

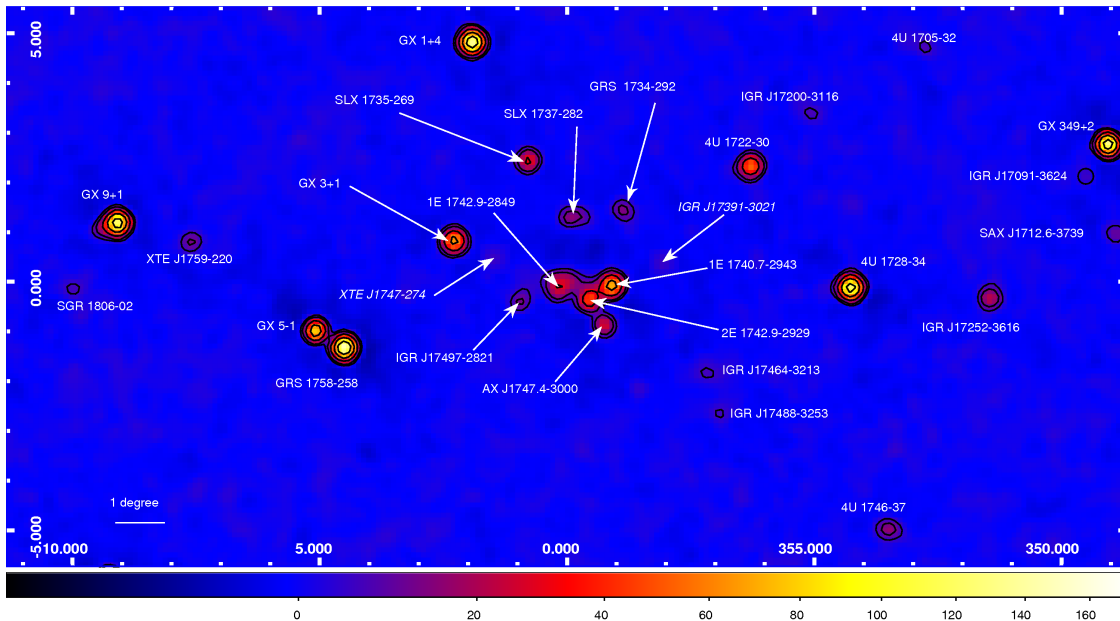


Fig. 4.— Significance image of the Galactic Center region as seen by Swift/BAT in the 15–55 keV band. Black contours denote levels of S/N which start from S/N = 4.8 and stop at S/N = 100 with a multiplicative factor of 2. The x and y axes show the Galactic longitude and latitude respectively.

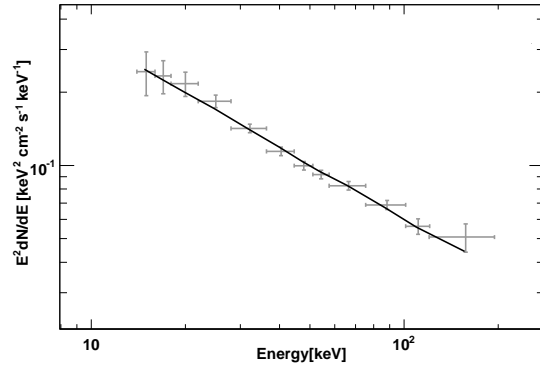
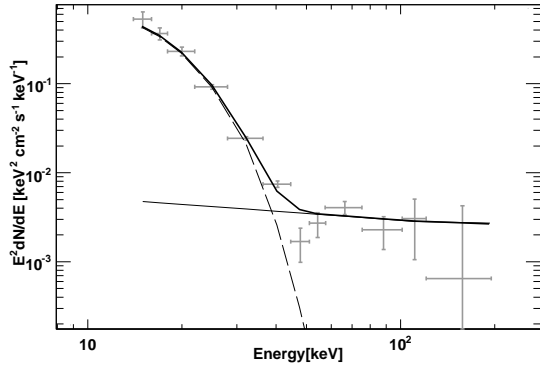


Fig. 6.— Average spectra of LMXB with $HR_2 > 0.6$ (left) and < 0.6 (right) respectively (see § 4 for a definition of the hardness ratio HR_2). The solid lines are the best fit models (power law plus black body for left and power law for right.)

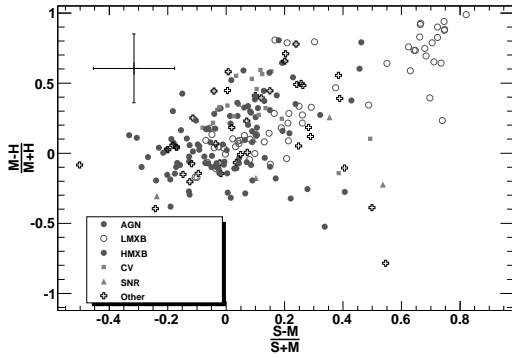


Fig. 5.— Hardness ratio plot of the BAT Galactic sample. In the upper left corner the typical $\pm 1\sigma$ error for a 5σ source is shown.

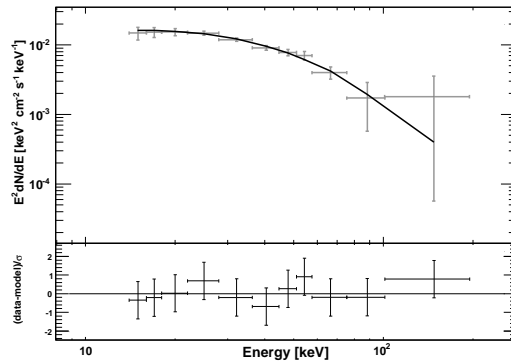


Fig. 7.— Stacked spectrum of the CVs detected by BAT. The solid line represent the best fit to the data (e.g. a bremsstrahlung model with a temperature of $22.68^{+2.39}_{-2.08}$ keV.)

5. Variability Analysis

To estimate the variability of the sources in our catalogue, we find numerical maximum-likelihood estimates of the intrinsic variability (Almaini et al. 2000) which has for example been used in the analysis of AGN from *XMM-Newton* (Mateos et al. 2007) and *Swift/BAT* (Beckmann et al. 2007) observations. In this method, the intrinsic variability σ_Q is found from solving

$$\sum_{i=0}^N \frac{(x_i - \bar{x})^2 - (\sigma_i^2 + \sigma_Q^2)}{(\sigma_i^2 + \sigma_Q^2)^2} = 0, \quad (3)$$

where x_i and σ_i are the measured count rate and error in each time bin i . As in Beckmann et al. (2007), we applied this method to the light curves with different time binnings of 1, 7, 20 and 40 days, and use the variability relative to the average count rate σ_Q/\bar{x} to estimate the strength of the variability. We simulated random light curves based on the observed source fluxes and errors. These were used to obtain Monte Carlo estimates of the errors on the calculated variabilities. We use both lightcurves generated at random positions and objects that are expected to be constant (supernova remnants) to investigate systematical effects caused by the instruments or the data analysis. For the random positions, we find an average variability of $\sigma_Q=6.0 \times 10^{-5}$, 1.1×10^{-5} , 4.5×10^{-6} and $2.5 \times 10^{-6} \text{ s}^{-1}$ for 1, 7, 20 and 40 days time binnings, respectively. From the supernova remnants, the systematic variability is seen to increase with increasing count rate, up to $\sigma_Q=1.4 \times 10^{-3}$, 9.7×10^{-4} , 9.0×10^{-4} and $5.9 \times 10^{-4} \text{ s}^{-1}$ for the Crab Nebula. To account for this, we subtracted the variability found at the random positions from the intrinsic variability of our sources. For the bright sources with count rates above 10^{-4} s^{-1} , we furthermore increased the error on the intrinsic variability, by $\sigma_{Crab} \times (\bar{x} - 1.0 \times 10^{-4} \text{ s}^{-1})$. In Fig. 8 we show the intrinsic fractional (σ_Q/\bar{x}) variability of the sources, as a function of the observed count rate, for the 7 day time binning. It is clear that almost all of the strongly variable objects belong to the Galaxy, and the vast majority of these are either HMXBs or LMXBs. Due to their soft spectra, only few stars and CVs are detected in the hard X-rays, and despite extra-Galactic sources being the most numerous source

class, they are almost entirely absent from the plot, as only a very small fraction of them are variable above the 10% level (Beckmann et al. 2007). Hard X-ray observations therefore have the potential to classify unidentified X-ray sources. For the sources with known distances, the luminosities can be derived. We caution that deriving distances to Galactic sources is inherently very uncertain and assumption-dependent. Only the bright globular cluster sources and a few very well studied binaries and SNR have distances known to a precision better than 10-20%, whereas the distances to some of the fainter sources can be uncertain by a factor of $\gtrsim 2$. We do not take the errors into account in our analysis. To significantly impact our conclusions, large systematical shifts (factor $\gtrsim 5$) of a high fraction of the sources would be necessary, which is unlikely. For the sources with calculated luminosities, we plot the variability as a function of source luminosity in Fig. 9. There is no obvious correlation between the luminosity and the strength of the variability (in the 1-40 days range). Note that the sensitivity decreases towards lower fluxes (but depends strongly on the specific observation pattern). This is the reason that the lower left parts of Fig. 8 and 9 are sparsely populated.

6. Source flux distributions

We use the average fluxes to calculate the source flux distributions for the different object types. The resulting logN-logS relations are shown in Figure 10. The sensitivity of the survey varies with direction and the sky coverage of our survey is shown in Figure 11. We have not corrected the logN-logS for the sky coverage, as such a correction depends on the expected spatial source distribution (see section 7 below for LMXBs and HMXBs). The lack of sources at low flux is therefore obviously caused by the strongly decreasing sky coverage below $\sim 2 \times 10^{-11} \text{ erg s}^{-1} \text{ cm}^{-2}$. It is clear that at high fluxes the two most important contributions are the HMXBs and the LMXBs, with the only exception being the Crab Nebula, which is the object with the highest flux in our sample. The third most important object type is the extra-Galactic sources, the contribution of which becomes important at fluxes below $10^{-10} \text{ erg s}^{-1} \text{ cm}^{-2}$. We note that limiting our survey to the Galactic plane strongly limits the importance of the extra-Galactic sources. Comparing

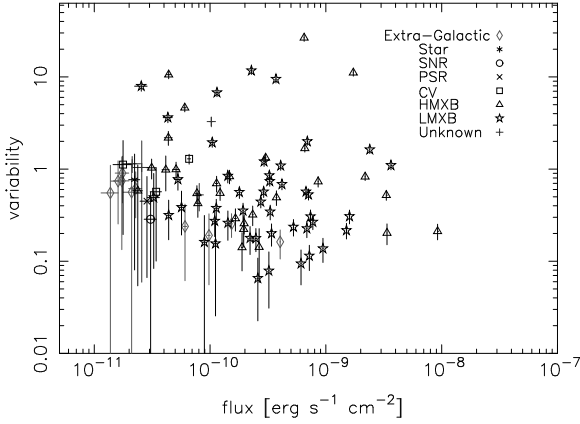


Fig. 8.— Intrinsic fractional variability (σ_Q/\bar{x}) of the sources, as a function of the observed count rate, for the 7 day time binning. Only objects with a variability greater than 2σ are included. For low count rates even sources with high variability are rejected by this criterion, and for this reason the lower left corner of the Figure is sparsely populated. The source types are defined in the catalogue, except for: Extra-Galactic, which is combined of the Seyfert, Blazar, Galaxy and Galaxy cluster types; Star, which covers Symbiotic stars, Be stars and a dwarf nova; Unknown, which are all objects not identified as any of the given types.

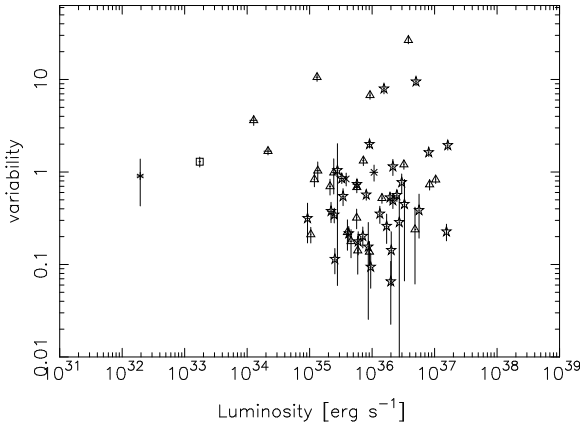


Fig. 9.— Intrinsic variability (σ_Q) of the sources, as a function of the observed luminosity, for the 7 day binning. Only objects with a variability greater than 2σ and with known distances are included.

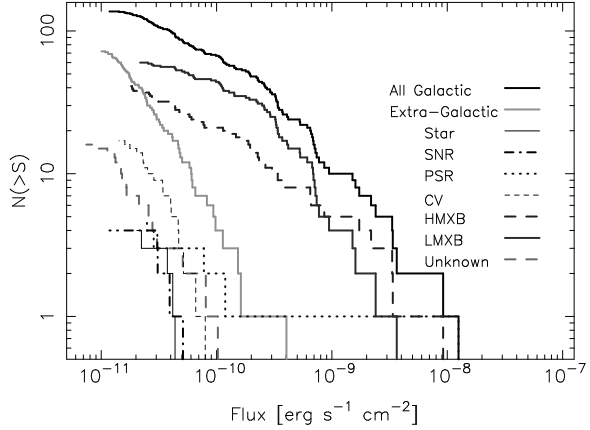


Fig. 10.— Cumulative logN-logS distributions of the observed sources.

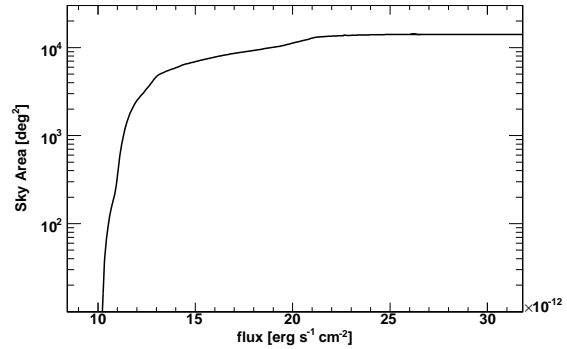


Fig. 11.— The sky coverage of the survey as a function of flux. The sensitivity depends on the local exposure and background, and is worse in the vicinity of bright sources. Above $\sim 2 \times 10^{-11}$ erg s^{-1} cm^{-2} the coverage quickly approaches a value of ~ 14000 deg^2 , corresponding to the full area within 20 deg of latitude from the Galactic plane.

Figure 10 to Figure 4 of Grimm et al. (2002), it can be seen that the relative importance of the HMXBs and the LMXBs is different in our 15-55 keV band to their results from the 2-10 keV band. In the hard X-rays, the HMXBs dominate the highest fluxes, with the LMXBs being more important at fluxes below 10^{-9} erg s $^{-1}$, whereas the LMXBs are always dominant in the soft X-rays. This is due to the fact that the luminous LMXBs have very soft spectra, and therefore emit almost negligible amounts of hard X-rays. For example Revnivtsev et al. (2008) found the typical ratio of hard (17-60 keV) to soft (2-10 keV) luminosities to be ~ 30 times lower for LMXBs with luminosities above 2×10^{37} erg s $^{-1}$ than for fainter LMXBs. A similar spectral break is not seen for the HMXBs.

7. Luminosity functions of X-ray binaries

For the majority of bright X-ray binaries in the Galaxy the distances are known within a factor of 2-3 (see discussion above). It is therefore possible to calculate the luminosity functions of the X-ray binaries. The other types of objects studied in this paper do not have adequate numbers of determined distances.

The sensitivity of the survey varies with the direction and the luminosity of the X-ray sources. Following Grimm et al. (2002) we account for this by setting up a model for the Galaxy and for the range of luminosities investigated we estimate the fraction of the Galaxy that is visible. As in Grimm et al. (2002), we use the three-component model of Bahcall & Soneira (1980) for the spatial distribution of the LMXBs, consisting of a disk, a bulge and spheroid. The parameters were chosen to fit the observed distribution of LMXBs (see equations 4–6 and Table 4 of Grimm et al. 2002), and the disk:bulge:spheroid mass ratios were chosen to be 2:1:0.8, where the mass of the spheroid is enhanced to account for the LMXBs formed in globular clusters. As the HMXBs are associated with the young stellar population in the Galaxy, only the disk component is considered relevant for the spatial distribution. To account for the spiral structure of the Galaxy, a spiral model based on optical and radio observations of giant HII regions (Georgelin & Georgelin 1976; Taylor & Cordes 1993) was assumed. This model consists of 4 spiral arms, which were assumed to have Gaussian density profiles along the Galactic

plane, with a width of 600 pc. The disk model was modulated by the spiral pattern: 20% for the LMXBs and 100% for the HMXBs.

For all directions we used the local background to estimate the limiting flux detectable by our survey, and used this to create a sensitivity map. For a given X-ray luminosity and direction, this enabled us to calculate the maximum distance, for which a X-ray binary is observable. However, to identify an X-ray source as an X-ray binary, and to determine the distance, it is necessary to have an optically identified counterpart. Grimm et al. (2002) estimated that above a distance of 10 kpc from the sun, the optical identification of X-ray binaries becomes incomplete. We adopt this result and limit our survey to this distance, irrespective of the X-ray brightness of the X-ray binaries. However towards the galactic bulge, source confusion and extinction are serious and optical/IR identifications are incomplete beyond $\sim 2 - 3$ kpc.

Combining the X-ray and optical limits with the model of the Galaxy, we estimate the fraction of the Galaxy observable as a function of source luminosity. This is shown in Fig. 12. Due to our distance constraints and sky coverage, even the brightest sources are limited to a part of the galaxy, and for this reason the lines do not reach a value of one.

The total Galactic luminosity functions of LMXBs and HMXBs are now found by correcting the observed luminosity functions for the fraction of the Galaxy probed by our survey. The outcome is shown for the LMXBs in Fig. 13 and the HMXBs in Fig. 14. Also shown in these figures are the luminosity functions obtained if the inner 10 deg of the bulge are excluded from our analysis, to assess the effects of source confusion. Obviously the luminosity function of the HMXBs is not affected, as these are not concentrated in the bulge. On the other hand, the luminosity function of the LMXBs is somewhat different with a lower normalization around 10^{36} erg s $^{-1}$. At both lower and higher luminosities the results are in agreement with the sample including the inner bulge. This is somewhat surprising as incompleteness due to a lack of optical IDs is expected to lead to the opposite effect, and could indicate a higher normalization of LMXBs per unit stellar mass in the bulge than in the disk. However, the statistical uncertainties,

together with the uncertainties of distance determination and the mass distribution of the Galaxy (both of which are difficult to quantify), are too large for such a conclusion to be significant. We note that recent results (Kim & Fabbiano 2010) indicate that the LMXB luminosity functions are age dependent at bright end ($> 10^{38}$ erg s $^{-1}$).

We use Maximum Likelihood (ML) fitting of broken power-laws to analyze the shape of the luminosity functions (using the full samples including the bulge). The resulting ranges and slopes are shown in Table 5. The faint slope of the LMXBs is slightly flatter than, but consistent with $\Gamma=1$, which is consistent with the INTEGRAL observations of the LMXBs in the Galactic bulge (Revnivtsev et al. 2008), and with the soft X-ray results of Gilfanov (2004); Voss & Gilfanov (2006, 2007). Due to the strong spectral change at luminosities of $\sim 10^{37}$ erg s $^{-1}$ (Revnivtsev et al. 2008), the LMXB luminosity function breaks and becomes very steep at higher luminosities. The HMXB fit gives a faint slope of $\gamma = -1.3^{+0.3}_{-0.2}$ for the HMXBs. This is somewhat shallower, but consistent with the ~ -1.6 slope found in the soft band both in the Milky Way (Grimm et al. 2002) and in other galaxies (Grimm et al. 2003). There is a clear break at luminosities above $\sim 2 \times 10^{37}$ erg s $^{-1}$, which is different from the single power-law shape seen in the soft X-rays. We note that the results are not strongly dependent on the few brightest sources. If the two brightest LMXB and HMXB sources are removed from our samples and the fits are repeated, the best-fit parameters are within the quoted errors.

7.1. Total luminosity

We find the combined luminosity from the Milky Way from summing all the sources with the individual incompleteness factors. This gives a hard X-ray luminosity of $1.3 \pm 0.6 \times 10^{38}$ erg s $^{-1}$ for the HMXBs and $1.7 \pm 0.4 \times 10^{38}$ erg s $^{-1}$ for the LMXBs. We note that the total emission is very dependent on the few brightest X-ray binaries (Gilfanov et al. 2004). The total luminosity can also be found by integrating the broken power-law fits to the observed sources, which gives $1.4^{+1.5}_{-0.3} \times 10^{38}$ erg s $^{-1}$ for the HMXBs and $1.5^{+1.5}_{-0.3} \times 10^{38}$ erg s $^{-1}$ for the LMXBs. For comparison, the luminosities in the soft band were found to be 2.0×10^{38} erg s $^{-1}$ for the HMXBs and

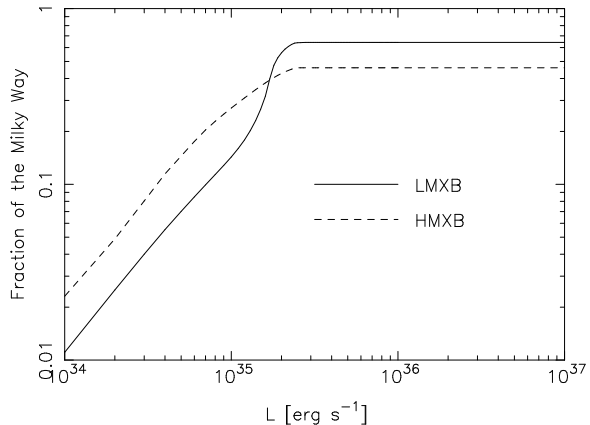


Fig. 12.— Fraction of the mass of the Galaxy probed by our survey, given the selection criteria described in the text.

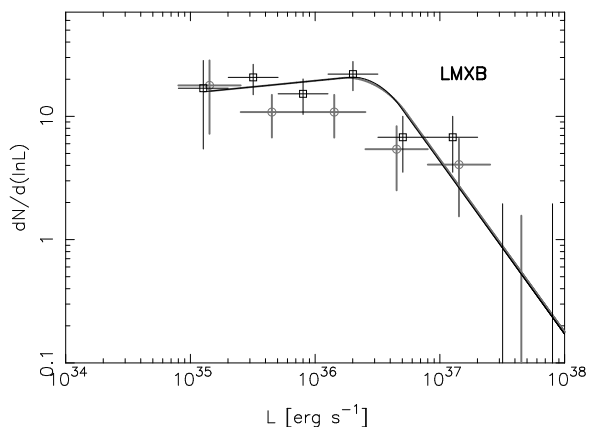


Fig. 13.— The luminosity function of Galactic LMXBs in the 15-55 keV band, corrected for incompleteness, with Poissonian errors. Squares indicate the results from the entire survey, whereas the inner 10 deg of the bulge were excluded for the circles. The solid black line shows the best maximum likelihood fit to the data from the entire survey, see Table 5.

2.5×10^{39} erg s⁻¹ for the LMXBs (Grimm et al. 2002). As the HMXBs have a relatively hard spectrum, the total luminosity in the 15-55 keV band is comparable to the soft luminosity, whereas the soft spectra of the brightest LMXBs causes their total hard band luminosity to be only 10% of the soft band luminosity. We note that, as above, the results from removing the brightest sources are within the quoted errors.

The number of HMXBs is roughly proportional to the star-formation rate of a galaxy (Grimm et al. 2003), whereas the LMXBs are related to the stellar mass of their host galaxy (Gilfanov 2004). The total luminosities should therefore be compared to the star-formation rate in the Milky Way estimated to be $2-4M_{\odot}$ yr⁻¹ (Diehl et al. 2006) and the stellar mass of $4.8 - 5.5 \times 10^{10} M_{\odot}$ (Flynn et al. 2006). From this we obtain the ratios: $L_x(\text{HMXB})/\text{SFR} \sim 3-7 \times 10^{37}$ erg s⁻¹ M_{\odot}^{-1} yr and $L_x(\text{LMXB})/M_{\text{stellar}} \sim 3 - 6 \times 10^{27}$ erg s⁻¹ M_{\odot}^{-1} .

A part of the diffuse X-ray background comes from X-ray sources in galaxies, and our results can be used to calculate the importance. The local stellar density is $M_* \sim 5 \times 10^8 M_{\odot} \text{Mpc}^{-3}$ (Salucci & Persic 1999; Cole et al. 2001), and the local star-formation rate is $\dot{\rho}_* = 0.015 M_{\odot} \text{Mpc}^{-3} \text{yr}^{-1}$ (Hanish et al. 2006). This gives a local emissivity from X-ray binaries of $\sim 2 - 4 \times 10^{36}$ erg s⁻¹ Mpc^{-3} , with approximately 80% coming from the LMXBs. This can be converted to incident flux I_{XRB} using equation 19 of Barcons et al. (1995). Assuming a normal galaxy density evolution of $(1+z)^3$, we find a flux of $1.5 - 3 \times 10^{-11}$ erg s⁻¹ cm⁻² Str⁻¹. We therefore conclude that the contribution to the hard X-ray background, which is 9.09×10^{-8} erg cm⁻² s⁻¹ sr⁻¹ (Ajello et al. 2008b), is negligible.

It should be noted that because of small-number statistics, the total X-ray luminosity of the HMXBs in a galaxy does not scale linearly with the star-formation rate (Grimm et al. 2003), except for galaxies with very high star-formation rates. The Milky Way might therefore provide a significant under-estimation of the actual L_x/SFR ratio. Indeed Grimm et al. (2002) found a ratio of $\sim 5 \times 10^{37}$ erg s⁻¹ M_{\odot}^{-1} yr, similar to our results, whereas Grimm et al. (2003) find an average ratio of 2×10^{39} erg s⁻¹ M_{\odot}^{-1} yr for a large sample

of galaxies². However, including this effect still limits the contribution to the X-ray background to $\lesssim 2\%$.

In the soft band galaxies have been found to contribute with $\sim 6-12\%$ of the X-ray background (e.g. Ranalli et al. 2005). This is a simple effect of the fact that the X-ray background is quite hard and so the X-ray binaries are on average softer. Furthermore in the hard band there is no contribution from the relatively soft X-rays from diffuse gas (e.g. Bogdán & Gilfanov 2008).

8. Discussion

Our analysis of the Galaxy in hard X-rays with the *Swift* BAT instrument shows that the most important sources are HMXBs and LMXBs, after which extra-Galactic sources start to dominate the observations. Compared to the Galaxy in softer X-rays, the contribution to the total luminosity from HMXBs is much higher, being $\sim 40\%$ in our observations, compared to $\lesssim 10\%$ in the 2-10 keV band (Grimm et al. 2002). This is mainly due to the fact that luminous LMXBs have very soft spectra, with only a few percent of the X-rays being hard. Soft X-rays from HMXBs have been found to be a good indicator of the star-formation rate in late-type galaxies (Grimm et al. 2003). Our observations show that hard X-rays can potentially be more useful for this purpose, especially in galaxies with mixed populations, due to the lower importance of LMXBs. Also in the hard band, possible contributions from hot X-ray emitting gas are avoided. We note that for nearby galaxies, where the brightest individual sources might be observed with future hard X-ray telescopes, the *number* of HMXBs provide a more reliable estimate of the star formation rate than the total luminosity. Extra-Galactic observations can be compared to our Milky Way estimates by integrating the luminosity function given in Table 5 down to the observational luminosity limit of the observed galaxy. At low luminosities, the background AGNs begin to dominate. It is therefore impossible to infer properties of the populations

²This value is different from the one listed in their paper. Shtykovskiy & Gilfanov (2005) discussed their star formation estimates and found that they corresponded to $\sim 1/3$ of the total star formation rate in the 0.1 - 100 M_{\odot} range.

of weaker sources, if optical counterparts have not been observed. This will only be possible with instruments with much better spatial resolution, where individual parts of the Galaxy can be studied in detail.

9. Conclusions

We have performed the first survey of the entire Galactic plane in X-rays, using the *Swift* BAT instrument in the 15-55 keV energy range. Out of the total 228 sources we identified the type of 211. The two most important contributions are the HMXBs and the LMXBs, both of which are also among the most variable objects in the Galaxy. The luminosity function of LMXBs is shown to be consistent with determinations from soft X-rays, and with previously results from a smaller sample observed with INTEGRAL. On the other hand, the slope of the luminosity function of HMXBs is more shallow than expected. Integrating the total luminosity of the X-ray binaries and extrapolating to other galaxies, we find that unresolved populations in galaxies contribute with a relatively small amount to the hard X-ray background.

This research has made use of data obtained from the High Energy Astrophysics Science Archive Research Center (HEASARC) provided by NASA's Goddard Space Flight Center, of the SIMBAD Astronomical Database which is operated by the Centre de Données astronomiques de Strasbourg, and of the ROSAT All Sky Survey maintained by the Max Planck Institut für Extraterrestrische Physik.

Facilities: Swift (BAT/XRT) .

REFERENCES

- Ajello, M., Greiner, J., Kanbach, G., Rau, A., Strong, A. W., & Kennea, J. A. 2008a, *ApJ*, 678, 102
- Ajello, M., et al. 2008b, *ApJ*, 689, 666
- . 2008c, *ApJ*, 673, 96
- . 2009, *ApJ*, 690, 367
- Almaini, O., et al. 2000, *MNRAS*, 315, 325
- Bahcall, J. N., & Soneira, R. M. 1980, *ApJS*, 44, 73
- Barcons, X., Franceschini, A., de Zotti, G., Danese, L., & Miyaji, T. 1995, *ApJ*, 455, 480
- Barthelmy, S. D., et al. 2005, *Space Science Reviews*, 120, 143
- Beckmann, V., Barthelmy, S. D., Courvoisier, T. J.-L., Gehrels, N., Soldi, S., Tueller, J., & Wendt, G. 2007, *A&A*, 475, 827
- Bird, A. J., et al. 2006, *ApJ*, 636, 765
- . 2007, *ApJS*, 170, 175
- Bogdán, Á., & Gilfanov, M. 2008, *MNRAS*, 388, 56
- Brinkmann, W., et al. 1997, *A&A*, 323, 739
- Brunschweiler, J., Greiner, J., Ajello, M., & Osborne, J. 2009, *A&A*, 496, 121
- Cole, S., et al. 2001, *MNRAS*, 326, 255
- Diehl, R., et al. 2006, *Nature*, 439, 45
- Flynn, C., Holmberg, J., Portinari, L., Fuchs, B., & Jahreiß, H. 2006, *MNRAS*, 372, 1149
- Gehrels, N., et al. 2004, *ApJ*, 611, 1005
- Georgelin, Y. M., & Georgelin, Y. P. 1976, *A&A*, 49, 57
- Gilfanov, M. 2004, *MNRAS*, 349, 146
- Gilfanov, M., Grimm, H.-J., & Sunyaev, R. 2004, *MNRAS*, 351, 1365
- Grimm, H.-J., Gilfanov, M., & Sunyaev, R. 2002, *A&A*, 391, 923
- . 2003, *MNRAS*, 339, 793
- Hanish, D. J., et al. 2006, *ApJ*, 649, 150
- Kaplan, D. L., Gaensler, B. M., Kulkarni, S. R., & Slane, P. O. 2006, *ApJS*, 163, 344
- Kim, D.-W., & Fabbiano, G. 2004, *ApJ*, 611, 846
- . 2010, *ArXiv:astro-ph/1004.2427*
- Kim, D.-W., et al. 2006, *ApJ*, 652, 1090
- . 2009, *ApJ*, 703, 829

- Krivonos, R., Revnivtsev, M., Lutovinov, A., Sazonov, S., Churazov, E., & Sunyaev, R. 2007, *A&A*, 475, 775
- Liu, Q. Z., van Paradijs, J., & van den Heuvel, E. P. J. 2005, *A&A*, 442, 1135
- . 2006, *A&A*, 455, 1165
- . 2007, *A&A*, 469, 807
- Lutovinov, A., Revnivtsev, M., Gilfanov, M., Shtykovskiy, P., Molkov, S., & Sunyaev, R. 2005, *A&A*, 444, 821
- Markwardt, C. B., Tueller, J., Skinner, G. K., Gehrels, N., Barthelmy, S. D., & Mushotzky, R. F. 2005, *ApJ*, 633, L77
- Mateos, S., Barcons, X., Carrera, F. J., Page, M. J., Ceballos, M. T., Hasinger, G., & Fabian, A. C. 2007, *A&A*, 473, 105
- Pietsch, W., Haberl, F., Sasaki, M., Gaetz, T. J., Plucinsky, P. P., Ghavamian, P., Long, K. S., & Pannuti, T. G. 2006, *ApJ*, 646, 420
- Ranalli, P., Comastri, A., & Setti, G. 2005, *A&A*, 440, 23
- Revnivtsev, M., Lutovinov, A., Churazov, E., Sazonov, S., Gilfanov, M., Grebenev, S., & Sunyaev, R. 2008, *A&A*, 491, 209
- Revnivtsev, M. G., et al. 2004, *Astronomy Letters*, 30, 382
- Salucci, P., & Persic, M. 1999, *MNRAS*, 309, 923
- Shtykovskiy, P., & Gilfanov, M. 2005, *A&A*, 431, 597
- Smith, D. M., Heindl, W. A., Markwardt, C. B., Swank, J. H., Negueruela, I., Harrison, T. E., & Huss, L. 2006, *ApJ*, 638, 974
- Taylor, J. H., & Cordes, J. M. 1993, *ApJ*, 411, 674
- Tueller, J., et al. 2010, *ApJS*, 186, 378
- Voges, W., et al. 1999, *A&A*, 349, 389
- Voss, R., & Gilfanov, M. 2006, *A&A*, 447, 71
- . 2007, *A&A*, 468, 49
- Voss, R., et al. 2009, *ApJ*, 701, 471
- Walter, R., et al. 2006, *A&A*, 453, 133
- Woodley, K. A., et al. 2008, *ApJ*, 682, 199
- Zhang, S., Chen, Y., Wang, J., Torres, D. F., & Li, T. 2009, *A&A*, 502, 231

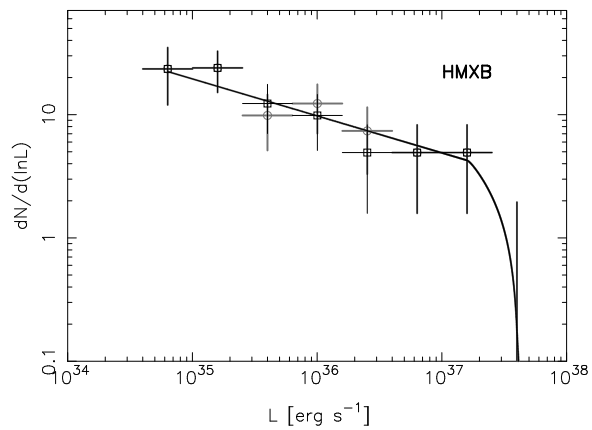


Fig. 14.— The luminosity function of Galactic HMXBs in the 15-55 keV band, corrected for incompleteness, with Poissonian errors. Squares indicate the results from the entire survey, whereas the inner 10 deg of the bulge were excluded for the circles. The solid black line shows the best maximum likelihood fit to the data from the entire survey, see Table 5.

TABLE 1
THE 228 DETECTED HARD X-RAY SOURCES

SWIFT NAME	R.A. (J2000)	Dec. (J2000)	σ (pos) (arcmin)	Flux (10^{-11} cgs)	S/N	ID	Type	Offset (arcmin)
J0018.8+8136	4.700	81.600	4.925	1.23	5.0	QSO J0017+8135	BLAZAR	3.7
J0024.9+6407	6.235	64.128	4.341	1.33	5.5	4U 0022+63	SNR	2.6
J0028.6+5918	7.162	59.301	2.063	6.11	25.0	V709 Cas	CV	1.4
J0035.7+5951	8.949	59.850	3.992	1.61	6.5	1ES 0033+59.5	BLLAC	1.1
J0055.2+4613	13.802	46.219	3.535	2.00	7.5	1RXS J005528.0+461143	CV	3.0
J0056.5+6042	14.127	60.705	2.544	7.11	28.6	Gam Cas	Be star	1.0
J0118.0+6517	19.503	65.293	0.948	15.45	64.3	4U 0114+65	HMXB	0.3
J0146.5+6144	26.635	61.745	3.158	2.49	9.7	PSR J0146+61	PSR	1.2
J0209.8+5227	32.453	52.453	3.727	2.75	9.9	SWIFT J0209.7+5226	Sy1	1.8
J0216.2+5126	34.051	51.449	4.090	1.69	6.0	SWIFT J0216.3+5128	Sy2	2.8
J0217.6+7351	34.402	73.851	4.838	1.56	6.3	SWIFT J0218.0+7348	BLAZAR	1.5
J0240.9+6115	40.233	61.266	4.462	1.90	7.2	2EG J0241+6119	HMXB	12.5
J0245.0+6228	41.266	62.473	4.233	4.67	17.9	QSO B0241+622	Sy1	0.8
J0257.3+4535	44.350	45.600	4.973	1.49	5.1
J0319.9+4131	49.982	41.522	2.736	6.89	23.1	NGC 1275	Sy2	1.5
J0324.9+3409	51.248	34.152	3.607	1.73	5.9	2MASX J03244119+3410459	Sy1	4.1
J0325.1+4042	51.299	40.700	5.082	1.60	5.4	UGC 2724	Sy2	5.1
J0331.2+4354	52.801	43.901	2.796	8.90	29.9	GK Per	CV	0.3
J0333.3+3718	53.350	37.300	3.411	1.48	4.9	IGR J03334+3718	Sy1	1.1
J0334.9+5310	53.746	53.173	0.412	83.32	314.1	V0332+53	HMXB	0.1
J0336.3+3219	54.086	32.330	3.602	1.73	5.8	4C 32.14	BLAZAR	2.4
J0355.3+3102	58.845	31.046	0.697	34.54	117.6	X Per	HMXB	0.2
J0418.4+3801	64.605	38.029	1.772	7.44	22.7	3C 111.0	Sy1	0.8
J0443.8+2857	70.950	28.952	5.243	2.40	6.6	UGC 3142	Sy1	1.2
J0444.1+2813	71.033	28.221	3.353	2.56	7.0	SWIFT J0444.1+2813	Sy2	0.3
J0452.1+4933	73.029	49.563	2.686	3.48	11.6	SWIFT J0452.2+4933	Sy1	1.0
J0457.2+4527	74.301	45.452	4.827	1.66	5.2
J0502.7+2445	75.699	24.753	4.029	2.03	5.4	Y1062 Tau	CV	1.8
J0502.8+2258	75.718	22.969	4.221	2.10	5.6	IRAS 04599+2255	Sy1	2.2
J0510.8+1630	77.718	16.500	2.905	5.17	13.9	CSV 6150	Sy1.5	1.6
J0534.5+2200	83.630	22.016	0.241	1267.31	3634.0	Crab	PSR	0.2
J0537.5+2106	84.399	21.100	6.090	1.88	4.9	zet Tau	Be*	3.2
J0538.9+2619	84.732	26.321	1.377	44.48	116.3	1A 0535+262	HMXB	0.1
J0542.6+6050	85.673	60.842	4.427	2.31	8.7	BY Cam	CV	1.4
J0552.2-0727	88.052	-7.459	1.192	16.11	43.7	NGC 2110	Sy2	0.3
J0554.9+4626	88.740	46.442	2.778	5.39	16.2	MCG +08-11-011	Sy1.5	0.7
J0557.8+5353	89.471	53.896	2.819	2.28	7.9	V405 Aur	CV	0.9
J0602.2+2828	90.553	28.482	3.448	3.80	9.0	SWIFT J0602.2+2829	Sy1	0.9
J0602.6+6522	90.669	65.369	3.800	1.38	5.4	UGC 3386	GALAXY	0.3
J0617.1+0908	94.291	9.138	0.600	35.35	88.7	4U 0614+091	LMXB	0.6
J0623.6-3214	95.901	-32.248	6.648	1.49	5.6	ESO 426-G 002	GALAXY-6dF	2.8
J0640.1-2554	100.034	-25.903	3.772	2.24	7.7	SWIFT J0640.4-2554	Sy1.2	1.0
J0655.8+3958	103.953	39.978	4.953	2.39	6.5	UGC 3601	Sy1	1.4
J0728.8-2606	112.224	-26.101	4.787	1.67	6.1	4U 0728-25	HMXB	0.4
J0731.4+0954	112.851	9.904	3.676	2.58	6.4	BG CMi	CV	2.5
J0732.6-1330	113.150	-13.504	3.140	2.86	8.8	SWIFT J0732.5-1331	CV	0.9
J0739.3-3143	114.849	-31.725	4.351	1.53	6.0	LEDA 86063	Sy2	4.4
J0746.1-1611	116.549	-16.199	5.432	2.12	7.2
J0748.5-6742	117.140	-67.714	0.894	19.26	85.4	EXO 0748-676	LMXB	2.2
J0751.0+0324	117.750	3.400	6.050	1.80	5.0	LEDA 97223	Sy1	3.3
J0751.1+1442	117.798	14.701	2.561	3.16	8.6	SWIFT J0750.9+1439	CV	2.7
J0759.7-3843	119.940	-38.732	3.071	2.84	12.0	IGR J07597-3842	Sy1.2	0.7
J0801.8-4946	120.453	-49.777	3.816	1.34	6.0	ESO 209-12	Sy1	1.4
J0804.1+0505	121.031	5.094	3.259	3.17	9.3	UGC 4203	Sy2	1.2
J0826.1-7030	126.531	-70.509	3.603	1.44	6.1
J0835.2-4511	128.808	-45.190	1.806	9.17	38.6	Vela Pulsar	PSR	1.4
J0838.3-3559	129.597	-35.998	4.216	2.09	8.8	Fairall 1146	Sy1	1.5
J0839.6-1214	129.900	-12.248	3.915	1.39	5.6	3C 206	Sy1	3.6

TABLE 1—*Continued*

SWIFT NAME	R.A. (J2000)	Dec. (J2000)	σ (pos) (arcmin)	Flux (10^{-11} cgs)	S/N	ID	Type	Offset (arcmin)
J0902.1-4033	135.529	-40.555	0.425	344.97	1727.0	Vela X-1	HMXB	0.3
J0902.5-4810	135.648	-48.177	3.912	1.36	5.5	IGR J09026-4812	...	2.9
J0916.1-6218	139.038	-62.308	5.416	1.84	7.4	SWIFT J0917.2-6221	Sy1	1.0
J0920.3-5511	140.092	-55.199	2.356	5.98	23.5	4U 0919-54	LMXB	0.8
J0923.9-3144	140.977	-31.742	3.498	1.69	6.9	2MASX J09235371-3141305	GALAXY6dF	3.0
J0947.5-3056	146.890	-30.947	1.746	11.34	43.1	ESO 434-40	Sy2	1.4
J1009.7-4250	152.450	-42.849	6.347	1.83	6.1	SWIFT J1009.3-4250	Sy2	2.2
J1009.8-5817	152.456	-58.293	2.045	6.26	23.1	GRO J1008-57	HMXB	0.5
J1010.9-5749	152.739	-57.827	3.248	2.03	7.3	SWIFT J1010.1-5747	STAR/Sym	1.6
J1031.7-3451	157.927	-34.861	2.108	5.10	15.7	NGC 3281	Sy2	2.0
J1038.6-4944	159.654	-49.749	4.510	1.80	5.8	SWIFT J1038.8-4942	Sy1	2.4
J1040.1-4624	160.041	-46.416	4.209	2.13	6.7	IGR J10404-4625	Sy2	2.2
J1121.2-6037	170.311	-60.624	0.698	89.14	397.8	Cen X-3	HMXB	0.2
J1131.1-6257	172.785	-62.957	2.673	4.75	15.8	IGR J11305-6256	HMXB	4.2
J1143.8-6106	175.967	-61.105	2.108	3.13	10.2	IGR J11435-6109	HMXB	2.7
J1147.4-6156	176.871	-61.949	1.204	24.15	80.5	1E 1145.1-6141	HMXB	0.3
J1202.6-5349	180.650	-53.820	4.514	2.47	7.8	SWIFT J1200.2-5350	Sy2	2.0
J1226.6-6246	186.658	-62.768	0.300	269.38	1012.8	GX 301-2	LMXB	0.1
J1234.7-6430	188.693	-64.504	2.968	4.32	13.6	IGR J12349-6434	STAR/Sym	3.8
J1249.4-5905	192.371	-59.099	2.567	6.33	19.6	4U 1246-58	LMXB	1.5
J1257.4-6915	194.365	-69.264	1.841	6.32	19.3	4U 1254-690	LMXB	1.7
J1300.8-6139	195.223	-61.656	3.808	1.86	5.7	GX 304-1	HMXB	4.3
J1301.7-6357	195.446	-63.951	2.229	4.20	12.8	IGR J13020-6359	HMXB	1.7
J1305.2-4928	196.318	-49.478	1.674	10.95	32.4	NGC 4945	Sy2	1.6
J1325.4-4300	201.363	-43.016	0.643	40.32	116.2	Cen A	Sy2	0.2
J1326.2-6207	201.575	-62.127	1.521	14.26	41.9	4U 1323-619	LMXB	2.2
J1347.5-6033	206.884	-60.566	2.193	4.76	13.5	4U 1344-60	Sy1	3.1
J1413.3-6518	213.337	-65.314	1.356	16.24	44.3	Cir Galaxy	Sy2	2.0
J1451.6-5537	222.916	-55.632	5.584	1.97	5.0	IGR J14515-5542	Sy2	2.9
J1453.6-5523	223.402	-55.400	6.204	2.01	5.0	IGR J14536-5522	CV	2.4
J1457.9-4305	224.500	-43.100	4.518	2.23	5.0	IC 4518	Sy2	3.3
J1514.1-5908	228.549	-59.145	1.169	11.89	29.4	PSR B1509-58	PSR	2.2
J1520.6-5710	230.153	-57.175	1.187	15.58	38.5	Cir X-1	LMXB	0.7
J1542.3-5222	235.592	-52.383	0.719	32.11	79.0	4U 1538-522	HMXB	0.3
J1547.9-6233	237.000	-62.554	2.861	5.87	14.2	4U 1543-62	LMXB	1.2
J1548.2-4529	237.053	-45.484	2.186	6.27	14.1	IGR J15479-4529	CV	0.5
J1601.1-6045	240.300	-60.766	5.361	2.29	5.5	1H 1556-605	LMXB	2.0
J1612.1-6034	243.049	-60.578	4.779	2.45	5.8	IGR J16119-6036	Sy1	4.1
J1612.7-5225	243.188	-52.422	1.190	40.98	111.8	4U 1608-522	LMXB	0.3
J1619.3-4944	244.829	-49.738	5.762	2.59	6.0	IGR J16195-4945	HMXB	2.2
J1619.6-2807	244.905	-28.124	3.311	4.17	8.4	IGR J16194-2810	STAR/Sym	0.9
J1620.8-5130	245.215	-51.508	3.779	2.95	6.8	IGR J16207-5129	HMXB	2.3
J1626.5-5156	246.645	-51.936	4.005	4.32	10.0	SWIFT J1626.6-5156	PSR	0.5
J1628.1-4912	247.027	-49.211	1.871	9.87	22.7	4U 1624-490	LMXB	1.0
J1631.8-4848	247.952	-48.816	1.027	37.44	91.3	IGR J16318-4848	HMXB	0.8
J1632.0-4752	248.015	-47.875	1.282	22.59	53.1	AX J1631.9-4752	PSR	0.3
J1632.3-6725	248.097	-67.422	1.165	26.13	62.3	4U 1626-67	LMXB	2.5
J1638.8-6423	249.714	-64.400	4.227	2.67	6.3	CIZA J1638.2-6420	GCluster	4.9
J1639.1-4642	249.798	-46.702	2.315	7.42	17.0	IGR J16393-4643	HMXB	2.2
J1640.9-5345	250.229	-53.755	0.752	42.21	106.1	4U 1636-536	LMXB	0.2
J1642.0-4532	250.506	-45.538	2.797	5.09	11.7	IGR J16418-4532	...	3.1
J1645.8-4536	251.451	-45.610	0.977	77.15	241.1	GX 340+0	LMXB	0.1
J1648.4-3035	252.108	-30.590	2.270	3.86	8.5	2MASX J16481523-3035037	Sy1	2.3
J1649.5-4350	252.395	-43.849	3.474	3.05	7.0	IGR J16493-4348	XBinary	3.4
J1651.8-5914	252.968	-59.239	4.347	2.29	5.3	ESO 138-1	Sy2	4.1
J1654.0-3950	253.500	-39.846	0.965	22.75	54.6	GRO J1655-40	LMXB	0.0
J1654.8-1920	253.701	-19.348	4.775	2.57	5.5	1RXS J165443.5-191620	...	4.7
J1656.2-3301	254.055	-33.031	3.544	3.01	6.8	SWIFT J1656.3-3302	BLAZAR	0.8

TABLE 1—*Continued*

SWIFT NAME	R.A. (J2000)	Dec. (J2000)	σ (pos) (arcmin)	Flux (10^{-11} cgs)	S/N	ID	Type	Offset (arcmin)
J1700.2-4221	255.056	-42.351	4.246	2.80	6.5	AX J1700.2-4220	HMXB	1.1
J1700.8-4139	255.203	-41.658	0.782	68.21	196.6	OAO 1657-415	HMXB	0.9
J1700.9-4611	255.246	-46.184	1.516	35.96	88.7	XTE J1701-462	LMXB	0.1
J1702.8-4847	255.707	-48.789	0.940	58.45	145.7	GX 339-4	LMXB	0.0
J1703.9-3750	255.987	-37.843	0.425	359.13	792.6	4U 1700-377	HMXB	0.2
J1705.7-3625	256.437	-36.423	0.568	94.45	328.3	GX 349+2	LMXB	0.1
J1706.3-6144	256.578	-61.745	3.843	2.78	6.4	IGR J17062-6143	TRANSIENT	2.7
J1706.2-4302	256.562	-43.040	1.134	29.03	71.0	4U 1702-429	LMXB	0.2
J1708.8-3218	257.202	-32.303	5.347	2.83	6.6	4U 1705-32	LMXB	1.5
J1708.8-4406	257.213	-44.113	1.170	32.79	80.3	4U 1705-440	LMXB	0.9
J1709.8-3626	257.450	-36.449	5.029	2.12	5.0	IGR J17091-3624	XR	8.8
J1710.2-2806	257.566	-28.111	3.773	3.26	7.6	XTE J1710-281	LMXB	1.5
J1712.3-2319	258.091	-23.324	2.895	8.51	19.7	Oph Cluster	GCluster	1.7
J1712.5-4050	258.146	-40.847	3.258	2.73	6.5	4U 1708-40	LMXB	2.3
J1712.6-3736	258.163	-37.611	4.146	4.44	10.6	SAX J1712.6-3739	LMXB	2.2
J1712.7-2417	258.181	-24.285	3.080	4.31	10.0	V2400 Oph	CV	2.9
J1717.0-6249	259.258	-62.833	2.148	6.17	14.3	NGC 6300	Sy2	0.9
J1719.7-4100	259.933	-41.009	2.882	3.42	8.2	1RXS J171935.6-410054	CV	1.6
J1720.2-3112	260.063	-31.214	4.073	2.75	6.6	IGR J17200-3116	HMXB	4.6
J1725.2-3617	261.303	-36.289	3.448	9.29	22.4	IGR J17252-3616	HMXB	0.5
J1727.5-3048	261.899	-30.806	2.335	22.15	53.6	4U 1722-30	LMXB	0.6
J1730.3-0559	262.599	-5.998	3.086	5.11	11.6	IGR J17303-0601	CV	0.6
J1731.7-1657	262.938	-16.950	0.826	37.29	90.2	GX 9+9	LMXB	0.7
J1731.9-3349	262.995	-33.829	0.626	67.38	195.5	4U 1728-34	LMXB	0.5
J1732.0-2444	263.016	-24.744	0.637	70.82	218.7	GX 1+4	LMXB	0.4
J1737.4-2908	264.375	-29.147	2.771	5.82	14.3	GRS 1734-292	Sy1	2.3
J1738.3-2659	264.578	-26.988	1.048	13.57	33.3	SLX 1735-269	LMXB	1.2
J1738.9-4427	264.749	-44.452	1.157	61.11	170.1	4U 1735-44	LMXB	0.3
J1740.4-2821	265.109	-28.357	5.578	6.48	15.9	SLX 1737-282	LMXB	7.3
J1743.9-2944	265.981	-29.738	1.759	32.53	84.0	1E 1740.7-2943	LMXB	0.5
J1745.9-2930	266.489	-29.500	2.083	19.27	46.4	2E 1742.9-2929	LMXB	2.0
J1746.2-3213	266.556	-32.225	4.290	3.06	7.6	IGR J17464-3213	LMXB	15.1
J1746.3-2851	266.598	-28.863	1.512	12.02	29.6	1E 1742.9-2849	LMXB	3.1
J1747.2-3001	266.811	-30.029	2.154	11.15	26.2	AX J1747.4-3000	LMXB	3.0
J1747.9-2633	266.993	-26.563	0.997	26.66	65.9	GX 3+1	LMXB	0.5
J1748.9-3257	267.230	-32.959	5.932	2.34	5.7	IGR J17488-3253	Sy1	2.8
J1749.6-2820	267.410	-28.348	2.433	10.25	26.0	IGR J17497-2821	...	0.4
J1750.2-3704	267.557	-37.072	2.833	6.54	15.9	4U 1746-37	LMXB	1.2
J1753.4-0126	268.373	-1.447	0.536	69.58	188.3	SWIFT J1753.5-0127	LMXB	0.5
J1759.8-2200	269.964	-22.007	2.538	5.28	13.1	XTE J1759-220	LMXB	1.3
J1801.1-2504	270.285	-25.079	0.956	193.47	475.2	GX 5-1	LMXB	0.1
J1801.2-2544	270.304	-25.740	0.810	68.51	213.6	GRS 1758-258	LMXB	0.2
J1801.5-2031	270.393	-20.522	0.536	53.03	140.9	GX 9+1	LMXB	0.6
J1808.6-2024	272.165	-20.417	5.660	2.85	7.1	SGR 1806-20	PSR	0.3
J1814.5-1708	273.628	-17.148	0.731	35.37	88.1	GX 13+1	LMXB	0.6
J1815.1-1205	273.784	-12.093	1.517	32.64	79.1	4U 1812-12	LMXB	1.1
J1816.0-1402	274.013	-14.037	0.278	199.08	546.7	GX 17+2	LMXB	0.4
J1817.6-3300	274.422	-33.011	1.614	10.44	25.4	XTE J1817-330	LMXB	0.6
J1821.4-1317	275.350	-13.300	4.370	2.06	5.0	IGR J18214-1318	...	0.7
J1823.6-3021	275.925	-30.360	1.093	76.69	250.2	4U 1820-30	LMXB	0.3
J1825.3-0001	276.345	-0.026	2.916	5.67	14.5	4U 1822-000	LMXB	0.8
J1825.8-3706	276.455	-37.106	0.858	44.39	107.6	4U 1822-371	LMXB	0.5
J1829.5-2347	277.378	-23.798	1.284	85.25	313.8	Ginga 1826-24	LMXB	0.6
J1833.5-1034	278.378	-10.582	2.643	4.36	10.5	SNR 021.5-00.9	SNR	1.4
J1833.7-2103	278.449	-21.053	4.978	2.76	6.6	PKS 1830-21	BLAZAR	1.9
J1834.9+3240	278.745	32.677	2.435	4.64	17.4	3C 382	Sy1	1.5
J1835.7-3259	278.938	-32.992	1.429	13.24	31.0	XB 1832-330	LMXB	0.2
J1837.9-0654	279.496	-6.916	4.031	3.09	7.5	HESS J1837-069	SNR	4.1

TABLE 1—Continued

SWIFT NAME	R.A. (J2000)	Dec. (J2000)	σ (pos) (arcmin)	Flux (10^{-11} cgs)	S/N	ID	Type	Offset (arcmin)
J1839.9+0502	279.997	5.039	0.586	34.47	99.7	Ser X-1	LMXB	0.5
J1841.4-0457	280.351	-4.950	3.486	3.07	7.6	SNR 027.4+00.0	SNR	1.5
J1845.6+0051	281.422	0.855	3.408	4.37	11.6	Ginga 1843+009	HMXB	2.3
J1846.4-0302	281.602	-3.046	3.900	2.49	6.3	PSR J1846-0258	PSR	4.3
J1848.2-0310	282.074	-3.174	3.532	5.32	13.4	IGR J18483-0311	PSR	0.7
J1853.0-0842	283.268	-8.703	1.962	8.94	21.3	4U 1850-086	LMXB	0.2
J1854.9-3109	283.733	-31.164	3.499	8.60	19.0	V1223 Sgr	CV	1.4
J1855.4-0236	283.875	-2.608	1.007	16.55	42.4	XTE J1855-026	HMXB	0.3
J1856.1+1536	284.050	15.600	5.688	1.39	4.8	2E 1853.7+1534	Sy1	3.6
J1858.8+0322	284.716	3.369	5.875	1.87	5.3	XTE J1858+034	HMXB	4.2
J1900.1-2453	285.029	-24.900	0.900	38.78	84.5	HETE J1900.1-2455	LMXB	1.3
J1901.6+0127	285.410	1.459	4.193	3.88	10.6	XTE J1901+014	HMXB	1.4
J1909.6+0950	287.415	9.837	1.641	21.74	71.8	4U 1907+09	HMXB	0.6
J1910.7+0735	287.693	7.594	1.916	19.64	61.2	4U 1909+07	HMXB	0.5
J1911.2+0034	287.816	0.581	2.092	11.48	32.2	Aql X-1	LMXB	0.2
J1911.7+0500	287.940	5.000	2.884	10.17	30.0	SS 433	HMXB	1.4
J1914.0+0952	288.525	9.883	1.428	11.40	37.4	IGR J19140+0951	HMXB	1.0
J1915.1+1056	288.795	10.945	1.030	380.66	1363.0	GRS 1915+105	LMXB	0.2
J1918.7-0514	289.690	-5.243	1.758	12.82	31.5	4U 1916-053	LMXB	0.6
J1920.9+4357	290.240	43.965	3.325	2.87	10.7	ABELL 2319	GCluster	2.2
J1922.5-1715	290.640	-17.266	2.235	9.61	20.0	SWIFT J1922.7-1716	XBinary	1.3
J1924.5+5016	291.131	50.268	3.487	2.23	8.3	CH Cyg	STAR/Sym	1.0
J1930.2+3411	292.568	34.184	2.895	1.75	6.8	SWIFT J1930.5+3414	Sy1	0.6
J1940.2-1024	295.052	-10.410	3.946	4.65	10.6	V1432 Aql	CV	0.9
J1942.5-1018	295.650	-10.306	3.809	4.77	10.9	NGC 6814	Sy1	1.5
J1943.9+2119	295.991	21.322	3.347	1.74	6.5	RX J1943.9+2118	...	1.8
J1949.5+3012	297.393	30.206	2.600	8.51	34.4	KS 1947+300	HMXB	0.8
J1955.6+3205	298.922	32.099	1.249	30.19	128.3	4U 1954+31	HMXB	0.3
J1958.3+3512	299.592	35.200	0.333	930.01	4123.6	Cyg X-1	HMXB	0.3
J1959.4+4044	299.865	40.735	2.369	6.48	24.4	Cyg A	Sy2	0.2
J1959.5+6509	299.889	65.159	2.973	2.53	10.2	2MASX J19595975+6508547	BLAZAR	2.9
J2000.3+3211	300.088	32.186	2.896	2.37	9.4	SWIFT J2000.6+3210	Be Star/HXB	0.3
J2018.5+4042	304.650	40.700	4.246	1.45	5.4	IGR J20187+4041	AGN	1.1
J2028.4+2544	307.121	25.743	3.447	3.47	13.1	MCG+04-48-002	Sy2	1.5
J2032.2+3738	308.065	37.638	0.321	196.91	573.9	EXO 2030+375	HMXB	0.1
J2032.4+4057	308.112	40.952	0.284	237.59	1012.0	Cyg X-3	HMXB	0.4
J2033.4+2144	308.354	21.749	3.788	1.67	6.2	XSS J20348+2157	GALAXY	2.2
J2036.9+4150	309.248	41.849	4.746	1.55	5.8	SWIFT J2037.2+4151	...	2.3
J2042.7+7508	310.678	75.137	2.577	3.28	13.5	4C +74.26	BLAZAR	0.4
J2056.6+4942	314.153	49.700	5.060	1.32	5.2
J2123.4+4216	320.853	42.277	5.518	1.43	5.6	V2069 Cyg	CV	4.0
J2124.5+5058	321.134	50.979	2.055	9.37	38.6	IGR J21247+5058	Sy1	1.2
J2127.4+5656	321.862	56.938	2.096	2.72	11.7	SWIFT J2127.4+5654	Sy1	2.5
J2133.6+5107	323.401	51.124	2.806	3.97	16.5	RX J2133.7+5107	CV	1.2
J2136.0+4730	324.018	47.512	4.468	1.44	5.9	RX J2135.9+4728	Sy1	2.8
J2138.5+3208	324.634	32.138	3.314	1.45	5.7	LEDA 67084	Sy1	3.2
J2142.6+4334	325.659	43.574	2.336	4.36	17.7	3A 2140+433	DWARF NOVA	2.9
J2144.6+3819	326.171	38.322	0.678	60.01	322.0	Cyg X-2	LMXB	0.0
J2202.8+4216	330.701	42.271	4.589	1.57	6.5	QSO B2200+420	BLLAC	1.0
J2208.0+5430	332.004	54.511	0.877	15.43	68.7	4U 2206+54	HMXB	0.8
J2245.5+3941	341.388	39.687	3.597	1.75	7.6	3C 452	Sy2	3.1
J2258.9+4051	344.730	40.863	3.257	1.36	5.9	UGC 12282	Sy1	4.2
J2307.8+4012	346.950	40.200	6.817	1.15	5.0	1RXS J230757.5+401636	...	5.0
J2323.2+5848	350.819	58.811	2.034	6.25	26.9	Cas A	SNR	1.0

TABLE 2
TENTATIVE ID FOR UNIDENTIFIED SOURCES

SWIFT NAME	R.A. (J2000)	Decl. (J2000)	S/N	ID	Type	Offset (arcmin)
J0457.2+4527	74.301	45.452	5.2	1RXS J045707.4+452751	AGN ^a	1.1
J0746.1-1611	116.549	-16.199	7.2	1RXS J074616.8-161127		1.3
J0826.1-7030	126.531	-70.509	6.1	1ES 0826-70.3		1.7
J2056.6+4942	314.153	49.700	5.2	RX J2056.6+4940	AGN ^b	2.0

^aThe extragalactic nature of 1RXS J045707.4+452751 has been proposed by Kaplan et al. (2006) on the basis of the hard X-ray spectrum and the X-ray-to-IR flux ratio.

^bThe nature of RX J2056.6+4940 is likely extragalactic because of its association with a radio-loud object (Brinkmann et al. 1997).

TABLE 3
NUMBERS OF DIFFERENT SOURCE TYPES IN OUR CATALOGUE.

CLASS	Number
LMXB	61
HMXB	43
CV	19
Supernova remnant	6
Pulsar	6
Star: symbiotic	4
Star: Dwarf Nova	1
AGN: Seyfert	56
AGN: BL Lac	2
AGN: Blazar	7
AGN: undefined	5
Galaxy cluster	3

TABLE 4

AVERAGE SPECTRAL PROPERTIES OF GALACTIC SOURCES DERIVED FROM THE ANALYSIS OF STACKED SPECTRA.

CLASS	N. Objects	Photon index	kT ^a (keV)
LMXB($HR_2 > 0.6$)	21	$2.25^{+0.83}_{-0.82}$	$2.7^{+0.19}_{-0.25}$
LMXB($HR_2 < 0.6$)	38	$2.74^{+0.06}_{-0.05}$...
HMXB	38	2.44 ± 0.05	...
CV	18	...	$22.68^{+2.39}_{-2.08}$
SNR	5	$1.84^{+0.32}_{-0.41}$	$6.23^{+3.80}_{-2.67}$

^aBest-fit temperature for a black-body model (LMXBs) or a bremsstrahlung model (CVs/SNRs)

TABLE 5

BROKEN POWER-LAW FITS TO THE LMXB AND HMXB LUMINOSITY FUNCTIONS

Type	Lum. limit	Nr.	Faint slope	Break	Bright slope	Total lum. ^a	Total luminosity ^b
LMXBs	8×10^{34}	81.4 ± 15.0	$0.9^{+0.4}_{-0.3}$	$3.0^{+1.8}_{-1.6} \times 10^{36}$	$2.4^{+0.4}_{-0.7}$	$1.7 \pm 0.4 \times 10^{38}$	$1.5^{+1.5}_{-0.3} \times 10^{38}$
HMXBs	4×10^{34}	73.1 ± 15.4	$1.3^{+0.2}_{-0.2}$	$2.5^{+2.0}_{-2.3} \times 10^{37}$	> 2	$1.3 \pm 0.6 \times 10^{38}$	$1.4^{+1.3}_{-0.3} \times 10^{38}$

^aFrom summing individual source luminosities corrected for incompleteness.

^bFrom integrating the fitted luminosity function.

